Solvothermal synthesis of lanthanide-functionalized graphene oxide nanocomposites

Acevedo-Guzmán, Diego A.; Huerta, Lázaro; Bizarro, Monserrat; Meza-Laguna, Víctor; Rudolf, Petra; Basiuk, Vladimir A.; Basiuk, Elena V.

Published in:
Materials Chemistry and Physics

DOI:
10.1016/j.matchemphys.2023.127840

Materials Chemistry and Physics 304 (2023) 127840

Contents lists available at ScienceDirect

Materials Chemistry and Physics

journal homepage: www.elsevier.com/locate/matchemphys

Solvothermal synthesis of lanthanide-functionalized graphene oxide nanocomposites

Diego A. Acevedo-Guzmán [a,b,*], Lázaro Huerta [c], Monserrat Bizarro [c], Víctor Meza-Laguna [d], Petra Rudolf [b], Vladimir A. Basiuk [d], Elena V. Basiuk [a,**]

[a] Instituto de Ciencias Aplicadas y Tecnología, Universidad Nacional Autónoma de México, Circuito Exterior C.U, 04510, Cd. México, Mexico
[b] Zernike Institute for Advanced Materials, University of Groningen, Nijenborgh 4, 9747 AG, Groningen, the Netherlands
[c] Instituto de Investigaciones en Materiales, Universidad Nacional Autónoma de México, Circuito Exterior C.U, 04510, Cd. México, Mexico
[d] Instituto de Ciencias Nucleares, Universidad Nacional Autónoma de México, Circuito Exterior C.U, 04510, Cd. México, Mexico

HIGHLIGHTS

- GO-Ln oxide/hydroxide (La,Eu,Gd,Tb) nanocomposites prepared by solvothermal method.
- Lanthanide oxide/hydroxide nanoparticles were formed on the graphene oxide surface.
- Ln oxides present better distribution and smaller sizes than Ln hydroxides.

GRAPHICAL ABSTRACT

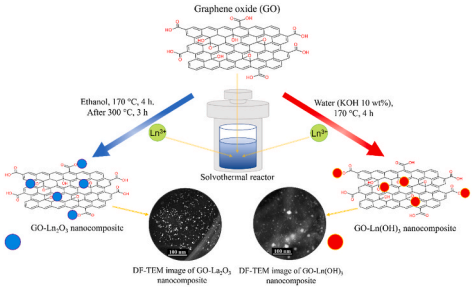

ARTICLE INFO

Keywords:
Graphene oxide
Lanthanides
Solvothermal synthesis
Nanocomposites
Characterisation

ABSTRACT

We propose a facile approach to the preparation of graphene oxide (GO) composites with lanthanide (Ln) oxide/hydroxide nanoparticles (Ln = La, Eu, Gd, Tb) under relatively mild conditions by two different procedures of solvothermal synthesis. The mechanism of GO-Ln nanocomposite formation is thought to involve the initial coordination of Ln^{3+} ions to the oxygen-containing groups of GO as nucleation sites, followed by f Ln_2O_3 and Ln $(OH)_3$ nanoparticle growth. The nanocomposites obtained preserve the intrinsic planar honeycomb-like structures of graphene as proven by the typical G and D bands in the Raman spectra. Fourier-transform infrared and X-ray photoelectron spectroscopy confirm the interaction between oxygen-containing groups of GO and Ln ions. The size and distribution of Ln oxide/hydroxide nanoparticles on GO sheets, estimated from scanning and transmission electron microscopy images, vary broadly for the different lanthanides. The size can span from sub-nm dimensions for Eu oxide to more than 10 μm for Eu hydroxide nanoparticles. The most homogeneous distribution of Ln oxide/hydroxide nanoparticles was found in La-containing composites. Thermogravimetric analysis demonstrated that all the GO-Ln nanocomposites are thermally less stable, by up to 30 °C than pristine GO.

* Corresponding author. Instituto de Ciencias Aplicadas y Tecnología, Universidad Nacional Autónoma de México, Circuito Exterior C.U, 04510, Cd. México, Mexico.
** Corresponding author.
E-mail addresses: d.a.acevedo.guzman@rug.nl (D.A. Acevedo-Guzmán), elena.golovataya@icat.unam.mx (E.V. Basiuk).

https://doi.org/10.1016/j.matchemphys.2023.127840
Received 17 January 2023; Received in revised form 27 March 2023; Accepted 28 April 2023
Available online 29 April 2023

1. Introduction

The graphene "gold rush" has resulted in the development of countless applications including electrochemical energy storage, sensors, and catalysts, using graphene (G) and graphene oxide (GO)-based materials. Surface functionalization with different metal species - single ions, neutral atoms or nanoparticles [1–3] - is a frequently explored approach to the development of metal-graphene composites. Among the most attractive metals are lanthanides, whose electronic configuration consists of filled [Xe]6*s* levels and 4f orbitals that are gradually filled as the atomic number increases. These 4f orbitals are strongly shielded from the external environment by the 5*s*5*p*6*s* orbitals, and therefore the ligands of lanthanide complexes cause only small perturbations in the 4f electron structure, and the lanthanides retain their properties [4]. Lanthanide ions are preferred dopants for diverse nanoparticles due to their outstanding properties such as stable luminescence, high fluorescence quantum efficiency and long luminescence lifetimes along with low toxicity [5–9]. The combination of the unique characteristics of carbon nanomaterials, in particular graphene, with those of lanthanides, opens a way to the preparation of novel materials with unusual magnetic, luminescent, catalytic, biological and other properties useful for a broad spectrum of applications in different areas of science, technology, and medicine [10–15].

Using graphene oxide as a solid support for lanthanide deposition can be advantageous because of the presence of oxygen-containing functional groups that promote the nucleation of metal-containing nanoparticles [16–21].

Many previously published works are focused on the interaction of lanthanide compounds with GO. However, most of them are limited to considering Ln ion and/or complex adsorption on different active sites, particularly the carboxylic groups of GO. Ashour et al. [22] reported the adsorption of La(III), Nd(III), Gd(III) and Y(III) ions as a dependent effect of the pH, because higher values of pH increase the degree of GO deprotonation and the negative charges on the GO surface promote the electrostatic interaction with Ln(III) ions. Narayanam et al. [23] studied the luminescence tunability of Eu(III) functionalized GO sheets in green and red wavelength regions but Eu(III) does not form nanoparticles, instead, its isolated ions bind with oxygen functionalities of GO. Pang et al. [24] designed and synthesized a luminescent terbium complex containing GO. In this case, Tb does not form nanoparticles, instead, it complexes with N2,N6-bis(4-aminobutyl)pyridine-2,6-cicarboxamide, forming a coordination compound, whose synthesis is a multi-step and ecologically unfriendly process. Wang et al. [25] described the preparation of Eu^{3+} and Tb^{3+} complex with GO for the detection of bacterial spores and cysteine, but first GO has to be covalently modified by grafting 1,2-Bis(2-aminoethoxy)ethane and ethylenediamine tetraacetic acid dianhydride (EDTAD) and later the coordination with Eu^{3+} and Tb^{3+} ions is achieved. Although these studies emphasise in adsorption and coordination of Ln(III) ions, reports on lanthanide-containing nanoparticles deposition onto GO (that is, on the synthesis of genuine GO-Ln nanocomposites) are much scarce. Jenkins et al. [26] and Jabeen et al. [27] reported the preparation of GO-Ln_2O_3 (namely Sm_2O_3, Dy_2O_3, Gd_2O_3, and Er_2O_3) nanocomposites showing AFM images revealing a particle size distribution in the nano range from 10 to 60 nm and agglomerates around 150 nm. Zhang et al. [28] synthesized a reduced GO/lanthanum oxide nanocomposite as an electrode material in a supercapacitor where La_2O_3 nanorods obtained have a diameter of about 20 nm utilising long-time heating reflux reaction. Aryanrad et al. [29] produced a GO/europium oxide nanorods nanocomposite where Eu nanorods present a diameter larger than 30 nm, but europium oxide nanorods have to be prepared previous their integration with GO as a self-assembly approach.

Subasri et al. [30] reported simple solvothermal reduction as a method to prepare a novel nanohybrid of $La(OH)_3$ electrostatically anchored onto 2D-graphene nanosheets and investigated as an electrode material for supercapacitors; unfortunately, this methodology required long reaction times, as well as DMF as reaction media and the previous preparation of $La(OH)_3$ nanoparticles, not to mention that it was tested only for lanthanum, and not for lanthanides having partially or totally filled 4*f* orbitals. Nanoparticle size in $La(OH)_3$/GO nanocomposite is around 7 nm and it is estimated by employing XRD, but it is not confirmed by microscopy studies (the use of transmission electron microscopy, TEM, is highly desirable or even mandatory). Sharma et al. [31] developed a hydrothermal method-assisted synthesis of Ce, Tb, and Ce/Tb-doped binary GO nanocomposites, using ionic liquid (1-butyl-3-methyl tetrafluoroborate) as reaction medium and fluorinating agents; the sizes of the reported nanoparticles are of 20–29 nm for CeF_3:Tb^{3+}-GO and LaF_3:Ce^{3+}/Tb^{3+}-GO and around 80 nm for BaF_2:Ce^{3+}-GO and BaF_2:Ce^{3+}/Tb^{3+}-GO nanocomposites.

Thus, the traditional synthetic routes for the preparation of composites based on carbon nanomaterials and lanthanides are carried out in an organic solvent, the amount of organic solvent used is large, compared with the amount of nanomaterial used, which is undesirable given the harmful effects on the environment and human health these solvents can produce. Other significantdisadvantages one should mention are elevated costs, difficulties in impurity removal, and special equipment requirements. For this reason, molten medium methods are a great alternative when it comes to developing more scalable, facile and efficient processes for different types of nanoparticles [32,33]. Furthermore, solvothermal synthesis is a well-known one-step technique for obtaining nanomaterials with high yields and at low cost. In addition to offering advantageous features like fast and uniform heating of the material and mild reaction conditions [34–39], this method can yield thermodynamically stable as well as metastable materials, which cannot be easily obtained through other synthetic routes. The ability to control the size and shape of target nanoparticles makes solvothermal synthesis especially valuable for applications in nanocircuits and devices. The process employs solvents under moderate to high pressure (typically between 1 and 10,000 atm) and temperature (typically between 100 °C and 1000 °C), which considerably facilitates the interaction of precursors during synthesis [40]. For example, Li et al. [41] employed solvothermal synthesis to decorate nitrogen-doped graphene with Fe_2O_3 and obtained uniformly dispersed and chemically bonded Fe_2O_3 nanocrystals that can be used as synergistic microwave absorbers. Another example is the synthesis of nanocomposites with carbon dots and Ag nanoparticles/TiO_2 studied by Wang et al. [42] to produce photocatalysts for environmental remediation.

However, in terms of an application of a broader variety of lanthanides and more environmentally friendly reaction media, the preparation of Ln-functionalized GO [30,31] deserve further exploration and improvements. Accordingly, the present study focuses on the solvothermal synthesis of lanthanide-functionalized graphene oxide nanocomposites. Two different preparation pathways for GO decorated with lanthanide oxide and hydroxide nanoparticles were tested for La, Eu, Gd and Tb. The nanocomposites obtained were characterized by several spectroscopic, microscopic, and thermal analysis techniques.

2. Experimental

2.1. Materials

La(III), Eu(III), Gd(III) and Tb(III) acetate hydrates (all having 99.9% purity), ethyl alcohol (CH_3CH_2OH, ≥99.5%), citric acid ($C_6H_8O_7$, ≥99.5%), and potassium hydroxide (KOH, ≥85%) were purchased from Sigma-Aldrich and used as received. Single-layer graphene oxide was purchased from Cheap Tubes, Inc. (>99 wt% purity, sheet size of 300–800 nm and thickness of 0.7–1.2 nm).

2.2. Solvothermal synthesis

Two series of GO-Ln nanocomposites were prepared using the solvothermal synthetic approach (see Fig. 1).

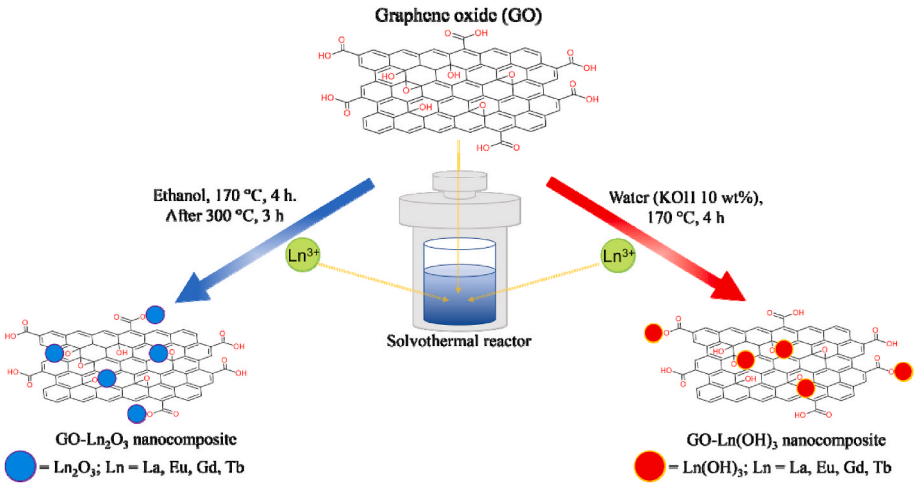

Fig. 1. Solvothermal synthesis employed for the preparation of GO-Ln oxides and hydroxides nanocomposites.

2.2.1. Series 1 labelled as GO-Ln-1

20 mg of GO was mixed with 2 mg of Ln(III) acetate hydrate in 10 mL of ethyl alcohol. The mixture was stirred for 5 min. Then, the solution was transferred to a Teflon-lined stainless-steel autoclave (25 mL) and heated at 170 °C for 4 h. Once the reaction was finished, the resulting mixture was dried under ambient conditions. The powder obtained was further heated at 300 °C for 3 h in air. The samples obtained are denoted hereafter as GO-La-1, GO-Eu-1, GO-Gd-1, and GO-Tb-1.

2.2.2. Series 2 labelled as GO-Ln-2

2 mg of Ln(III) acetate hydrate and 0.25 mmol of citric acid were dissolved in 20 mL of deionized water. At the same time, also a 10 mL aqueous solution containing 10 wt% potassium hydroxide and 20 mg GO was prepared. The lanthanide solution was added to the KOH solution and stirred for 5 min. The prepared mixture was transferred to a Teflon-lined stainless-steel autoclave (50 mL) and heated at 170 °C for 4 h. Once the reaction was finished, the product was centrifuged to collect the solid phase, which was washed three times with deionized water (this methodology was adapted from the one described in Ref. [43]). The samples obtained are denoted hereafter as GO-La-2, GO-Eu-2, GO-Gd-2, and GO-Tb-2.

2.3. Characterisation

Raman spectral characterisation was performed on a Raman Witec alpha300R (WITec GmbH, Ulm, Germany) using a 532 nm wavelength laser light excitation from a Nd:YVO4 laser. The incident laser beam with a power of 2.85 μW was focused on the sample using a 100x objective (Zeiss, 0.9 NA). Ten punctual Raman spectra of every sample were collected randomly, in a Raman shift range of 500–4000 cm^{-1}. Each spectrum was the average of 60 scans collected at 0.5 cm^{-1} resolution. Fourier-transform infrared (FTIR) spectra were recorded in the range 500–4000 cm^{-1} on a Nicolet iS50R Thermo-Scientific spectrometer, under ambient conditions. Each spectrum was the average of 32 scans collected at 4 cm^{-1} resolution.

X-Ray photoelectron spectroscopy (XPS) measurements were carried out on two instruments:

(1) a Scanning XPS microprobe PHI5000 VersaProbe II system, equipped with a monochromatic Al Kα X-ray source ($h\nu = 1486.6$ eV); the pressure in the chamber was maintained at 7×10^{-10} mbar during data acquisition and the electron take-off angle with respect to the surface normal was 45°. The XPS data were acquired by using a spot size of 100 μm in diameter and the energy resolution was 0.56 eV for the detailed spectra of core level regions; the programs PHI Multipack© version 9.6.0.15 and SDP© v 4.1 were employed for the deconvolution analysis;

(2) a Surface Science Instruments SSX-100 ESCA instrument with a monochromatic Al Kα X-ray source ($h\nu = 1486.4$ eV); the pressure in the chamber was maintained at 1×10^{-9} mbar during data acquisition and the electron take-off angle with respect to the surface normal was 37°. The XPS data were acquired by using a spot size of 1000 μm in diameter and the energy resolution was 1.3 eV for the detailed spectra of core level regions; XPS spectra were analyzed using the least-squares curve-fitting program Winspec (developed at the LISE laboratory of the University of Namur, Belgium).

For both measurements, powder samples were dispersed in isopropanol, sonicated for 5 min, and dop-casted on a thin gold film, grown on mica. Peak profiles were taken as a convolution of Gaussian and Lorentzian functions and Shirley background was used; binding energies (BEs) were referenced to the Au $4f_{7/2}$ photoemission peak [44] centered at 84.0 eV and accurate to ± 0.1 eV when deduced from the fitting procedure. The uncertainty in the peak intensity determination is within 2% for all core levels reported. All data were normalized to the number of scans and corrected for the sensitivity factor of the spectrometer. The transmission function of the analyser was corrected by the Atomic Sensitivity Factor (ASF) reported by Scofield [45] with the lanthanides reference materials. All measurements were carried out on freshly prepared samples.

The powder X-ray diffraction (XRD) patterns were collected on a D8 Advance Bruker diffractometer in Bragg-Brentano geometry with a monochromatic Cu Kα X-ray source (wavelength of 1.5418 Å) and a Lynxeye detector. Powder samples were first placed on a zero-background holder. The patterns were recorded in a 2θ range from 5 to 70°, in steps of 0.02° and with a counting time of 0.75 s per step.

For scanning electron microscopy (SEM) characterization of the samples, we used a JEOL JSM-6510LV microscope and backscattered mode was employed, operated at a voltage of 20 kV. The SEM instrument was coupled to an INCA Energy 250 Energy Dispersive X-ray (EDS) Microanalysis System from Oxford Instruments. For acquiring the dark-field transmission electron microscopy (DF-TEM) images, a JEOL JEM-ARM200F STEM (Schottky field emission gun) instrument was used, operated at 1.0 Å resolution and 200 kV voltage. Samples were dispersed in isopropanol, sonicated for 5 min, and drop-casted using standard grids with collodion support films.

Thermogravimetric (TGA) and differential thermal analysis (DTA) were performed on an STD 2960 Simultaneous DSC-TGA analyser from TA Instruments in air; the airflow was 100 mL/min and a heating ramp

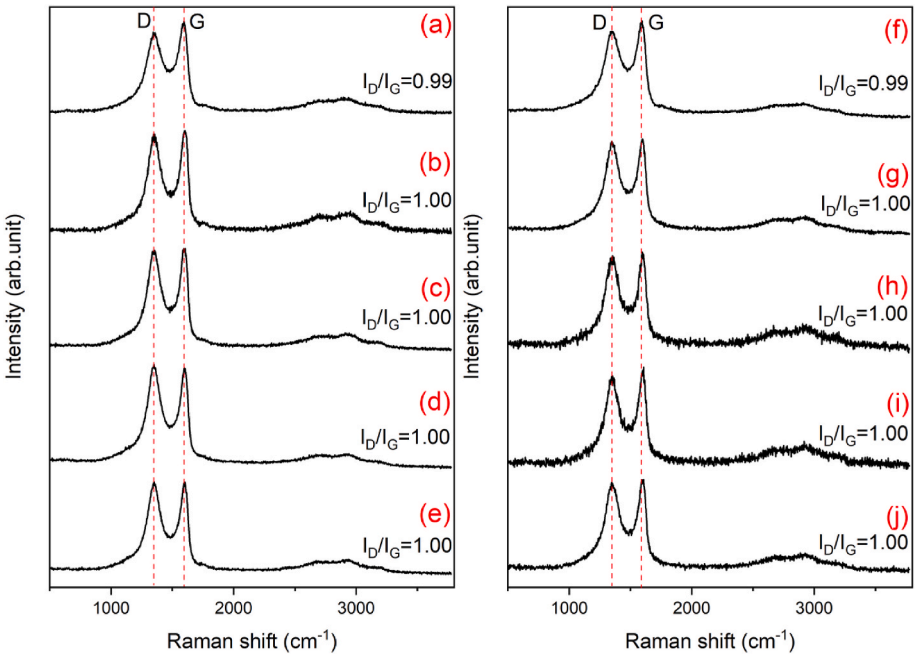

Fig. 2. Comparison of the Raman spectra for (a, f) pristine GO, (b) GO-La-1, (c) GO-Eu-1, (d) GO-Gd-1, (e) GO-Tb-1, (g) GO-La-2, (h) GO-Eu-2, (i) GO-Gd-2, and (j) GO-Tb-2.

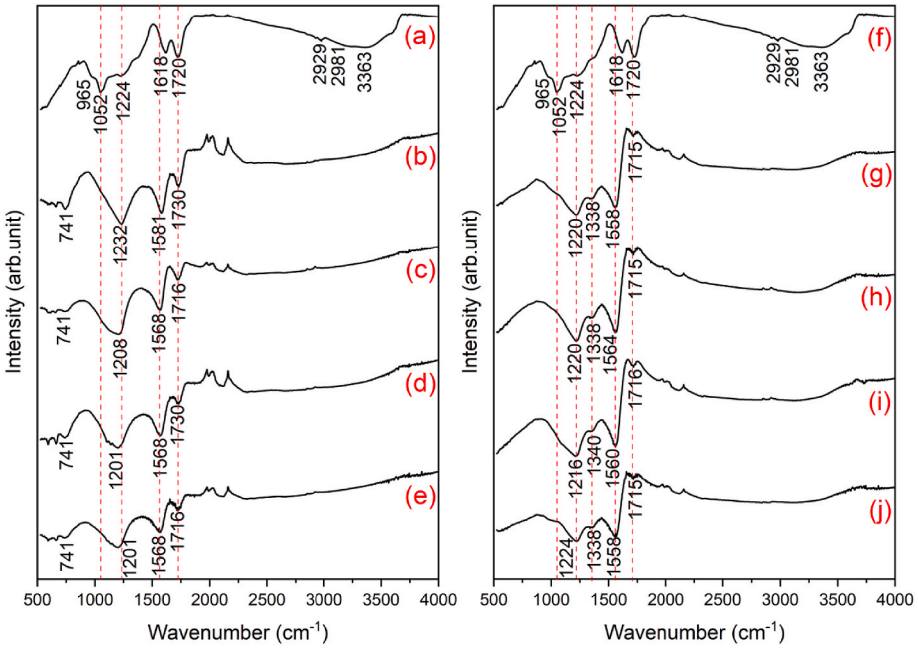

Fig. 3. Comparison of FTIR spectra of (a, f) pristine GO, (b) GO-La-1, (c) GO-Eu-1, (d) GO-Gd-1, (e) GO-Tb-1, (g) GO-La-2, (h) GO-Eu-2, (i) GO-Gd-2, and (j) GO-Tb-2.

of 10 °C/min up to 1000 °C was applied. Samples of approximately 5 mg were used.

3. Results and discussion

Detailed information on the composition, morphology, and structure of the nanohybrid materials was obtained from FTIR, Raman, EDS and XPS spectroscopy, XRD, SEM and HRTEM microscopy, as well as TGA and DTA thermal analysis.

The Raman spectra of all samples (Fig. 2) showed the presence of the characteristic D band centered at about 1350 cm^{-1}, which is related to C-C bond disorder (sp^3-hybridized carbon atoms), and the G band located at 1595 cm^{-1}, which is caused by stretching vibrations of C═C of the sp^2 hybridized carbon backbone [46–49]. For both series, the ratio between D and G band intensities (I_D/I_G) did not exhibit tangible changes from 0.99 for pristine GO to 1.00 for all GO-Ln hybrids, thus implying that the solvothermal treatment nor the interaction of lanthanide ions with the GO affect the ratio between sp^3-and sp^2-hybridized carbon atoms.

At the same time, the FTIR analysis (Fig. 3) revealed evident changes upon the solvothermal chemical modification of GO sheets. Pristine GO showed typical peaks due to the presence of oxygen-containing functional groups [50,51]: the broad stretching hydroxyl ν_{OH} band at 3363 cm^{-1} and the corresponding deformation δ_{OH} band at 1618 cm^{-1},

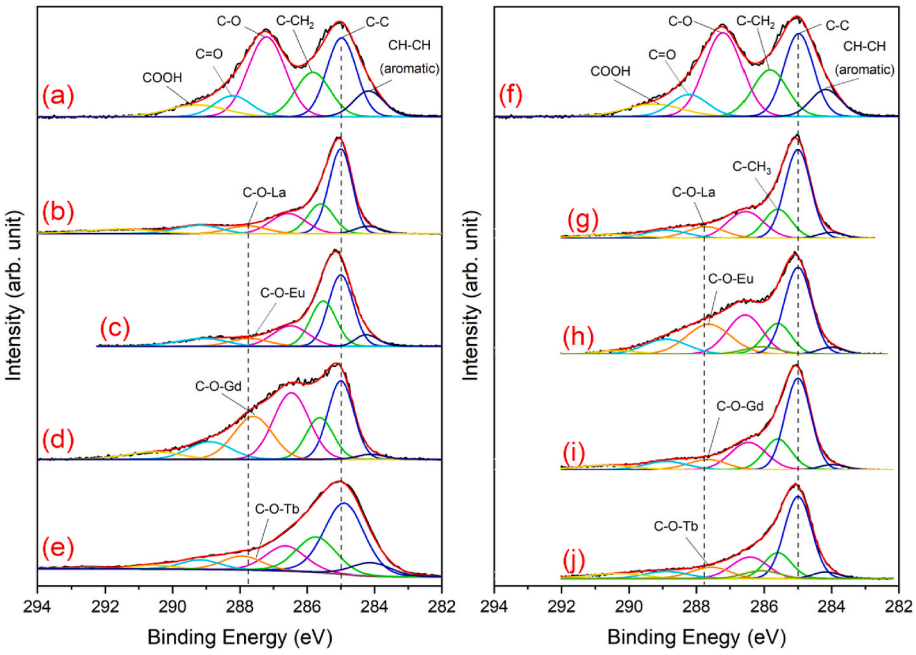

Fig. 4. Comparison of XPS spectra of the C1s core level region of (a, f) pristine GO, (b) GO-La-1, (c) GO-Eu-1, (d) GO-Gd-1, (e) GO-Tb-1, (g) GO-La-2, (h) GO-Eu-2, (i) GO-Gd-2, and (j) GO-Tb-2 and corresponding fits.

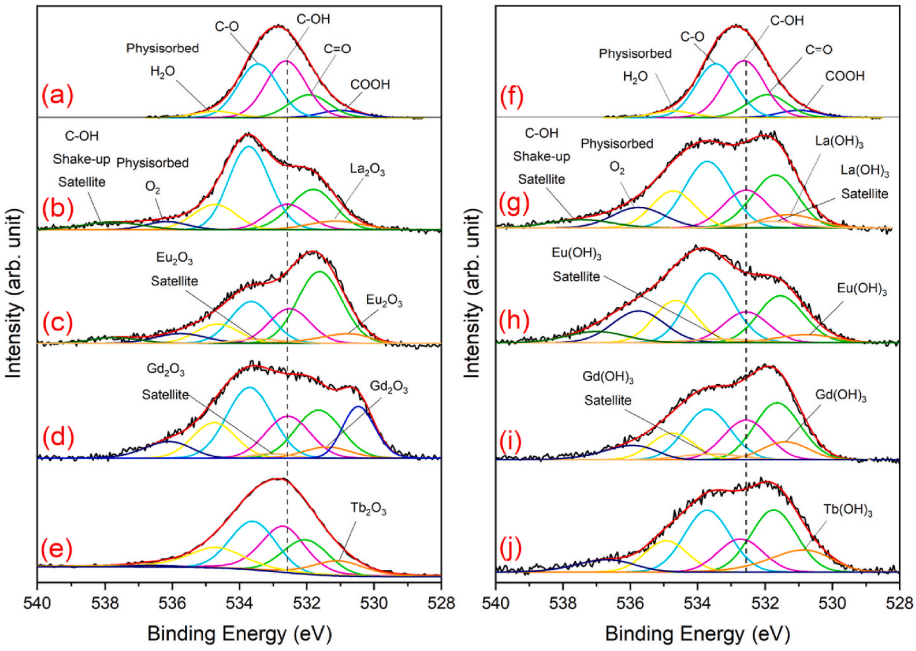

Fig. 5. Comparison of the XPS spectra of the O1s core level region of (a, f) pristine GO, (b) GO-La-1, (c) GO-Eu-1, (d) GO-Gd-1, (e) GO-Tb-1, (g) GO-La-2, (h) GO-Eu-2, (i) GO-Gd-2, and (j) GO-Tb-2 and corresponding fits.

stretching $\nu_{C=O}$ vibrations in COOH groups at 1720 cm^{-1}, a strong band at 1224 cm^{-1} due to asymmetric and symmetric stretching modes of epoxy C-O-C groups, a band at 1052 cm^{-1} associated with C-O stretching vibrations, and a shoulder at 965 cm^{-1} due to unsaturated ketone groups. A weak symmetric and asymmetric ν_{C-H} bands at 2981 and 2959 cm^{-1} and a signal of unoxidized sp^2 C=C bonds at 1552-1593 cm^{-1} can be observed as well.

While in the FTIR spectra of GO-Ln samples for both Series 1 and 2, the intensity of the broad hydroxyl ν_{OH} stretching band at 3363 cm^{-1} significantly decreased, and some differences were found depending on the particular synthetic approach. The most noticeable changes observed for the samples of Series 1 were the frequency shift of the epoxy band to 1232 cm^{-1} for GO-La-1, 1208 cm^{-1} for GO-Eu-1, and 1201 cm^{-1} for both GO-Gd-1 and GO-Tb-1, indicating an epoxide ring opening reaction. Fig. 2 shows a decrease in the intensity of the COOH band and an almost total disappearance of the C-O signal at 1052 cm^{-1} for all GO-Ln-1 samples. On the other hand, one can see an intensity increase for the band corresponding to the vibrations of unoxidized sp^2 C=C bonds at 1568-1581 cm^{-1}, as well as emerging bands at 724-550 cm^{-1} related to the Ln-O vibrations. For the Series 2 samples, the epoxy band (~1220 cm^{-1}) increased in intensity and became broader. In addition, the band intensity due to the COOH group decreased, along

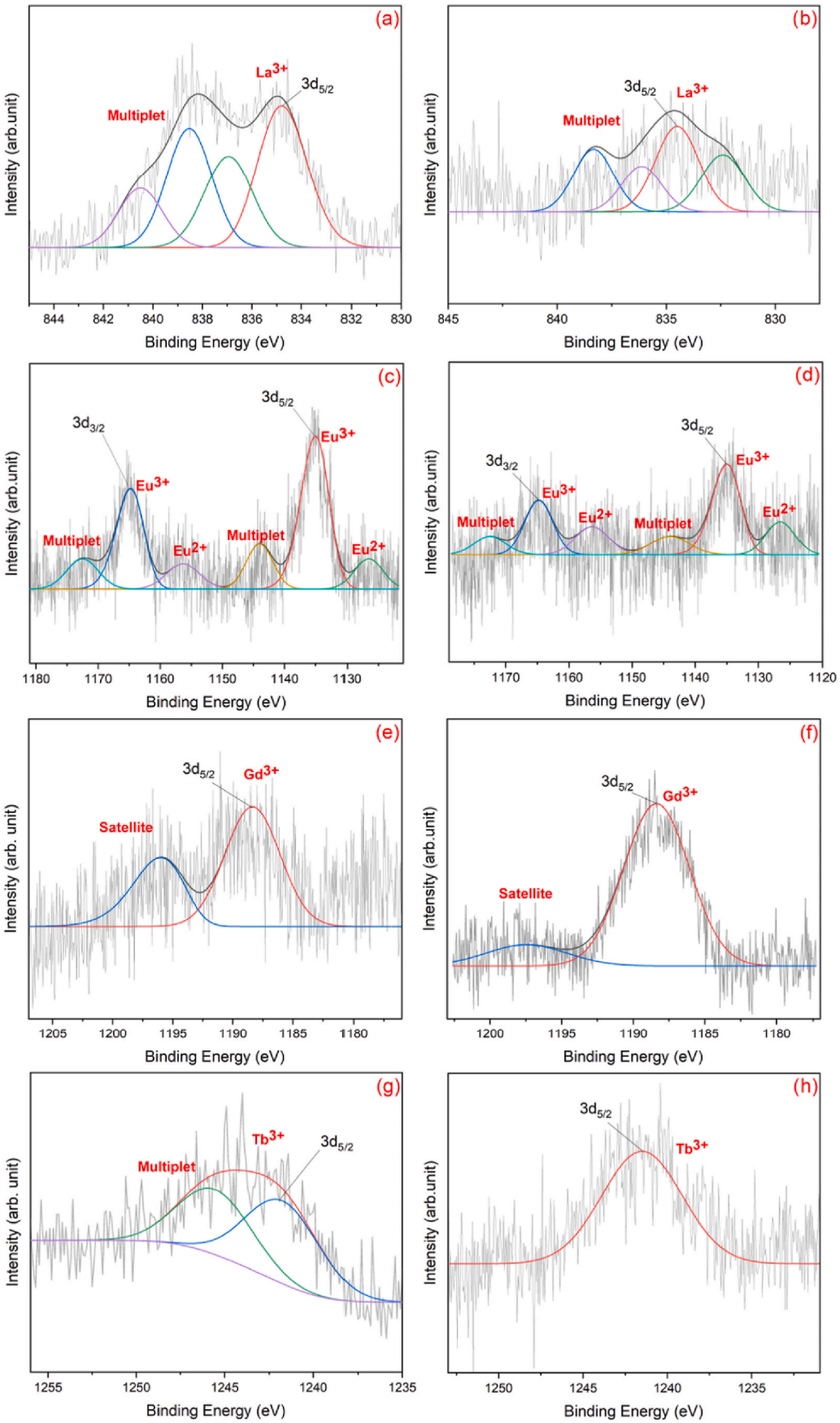

Fig. 6. Comparison of the XPS spectra of the Ln 3d core level region of (a) GO-La-1, (b) GO-La-2, (c) GO-Eu-1, (d) GO-Eu-2, (e) GO-Gd-1, (f) GO-Gd-2, (g) GO-Tb-1 and (h) GO-Tb-2 and corresponding fits.

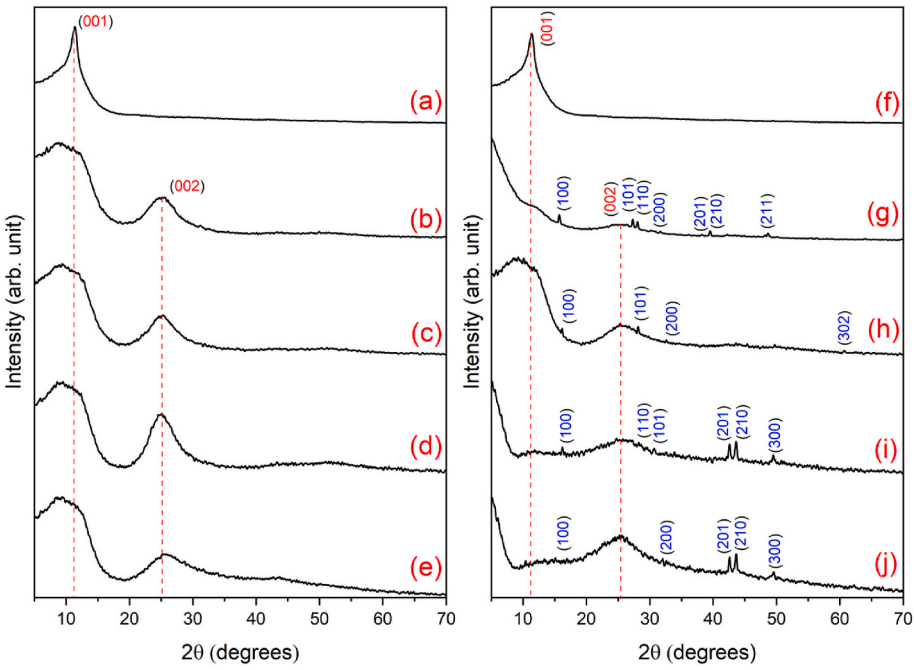

Fig. 7. Comparison of XRD diffractograms of (a, f) pristine GO, (b) GO-La-1, (c) GO-Eu-1, (d) GO-Gd-1, (e) GO-Tb-1, (g) GO-La-2, (h) GO-Eu-2, (i) GO-Gd-2, and (j) GO-Tb-2. (Red numbers correspond to GO peaks and blue numbers correspond to lanthanide hydroxides peaks). (For interpretation of the references to colour in this figure legend, the reader is referred to the Web version of this article.)

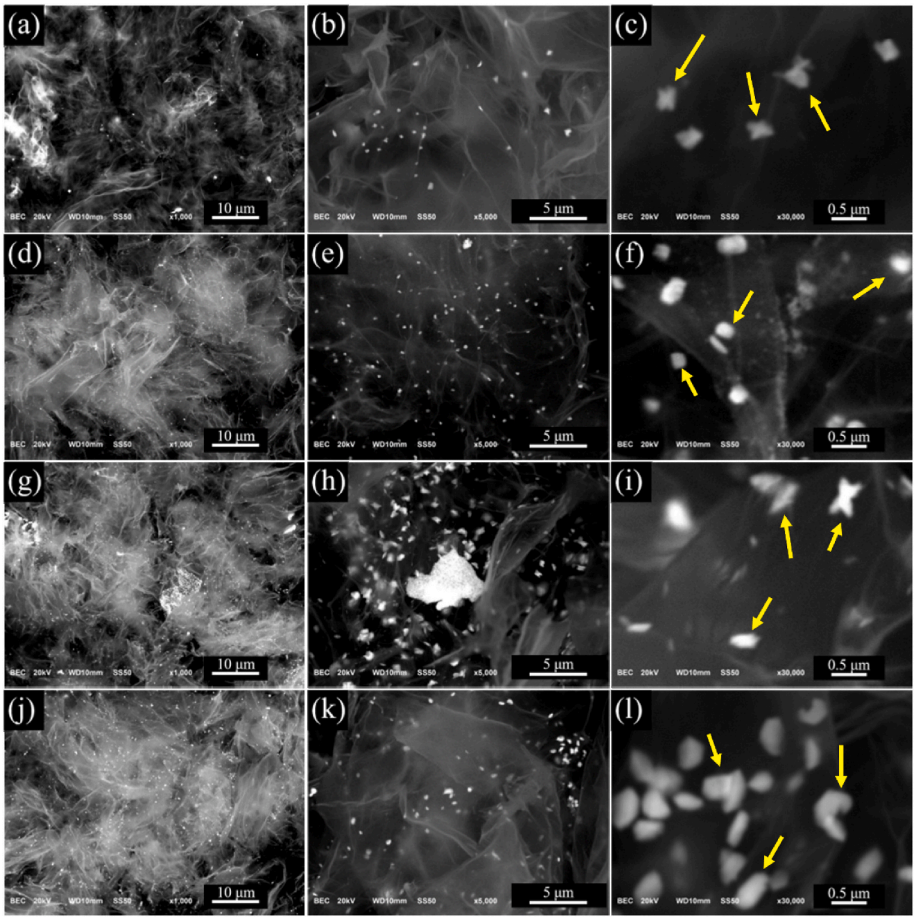

Fig. 8. SEM-BEC images at different magnifications of (a–c) GO-La-1, (d–f) GO-Eu-1, (g–i) GO-Gd-1, and (j–l) GO-Tb-1. (Yellow arrows point to lanthanide oxide particles). (For interpretation of the references to colour in this figure legend, the reader is referred to the Web version of this article.)

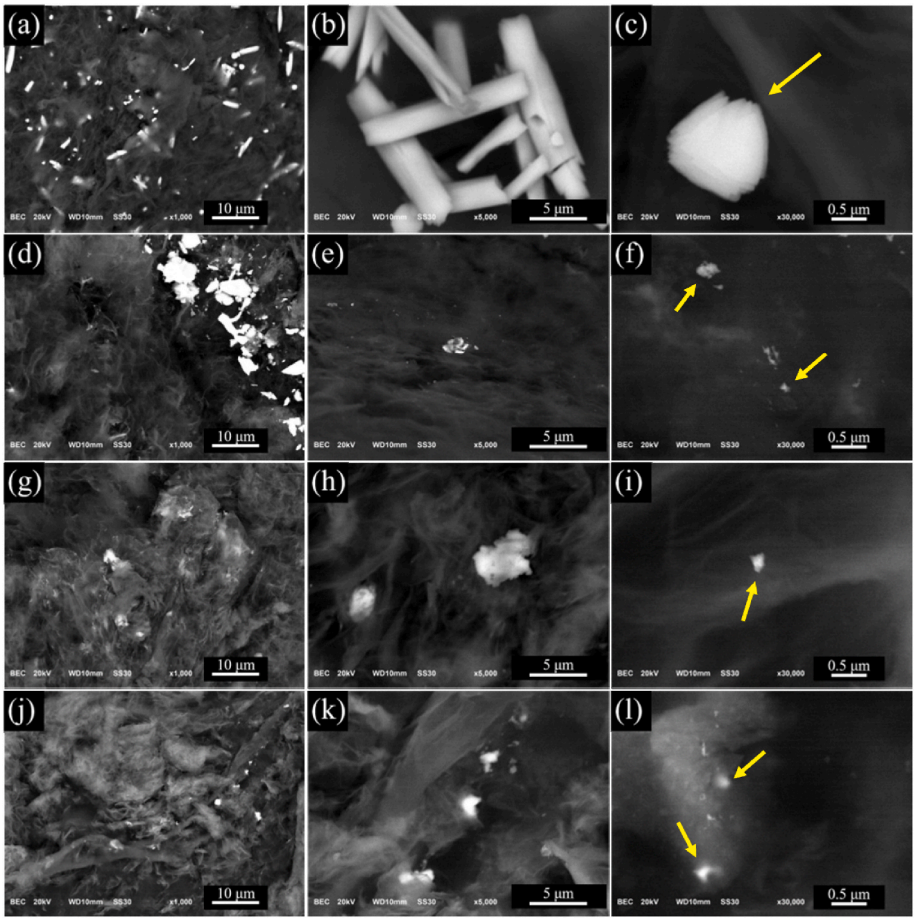

Fig. 9. SEM-BEC images at different magnifications of (a–c) GO-La-2, (d–f) GO-Eu-2, (g–i) GO-Gd-2, and (j–l) GO-Tb-2. (Yellow arrows point to lanthanide hydroxide particles). (For interpretation of the references to colour in this figure legend, the reader is referred to the Web version of this article.)

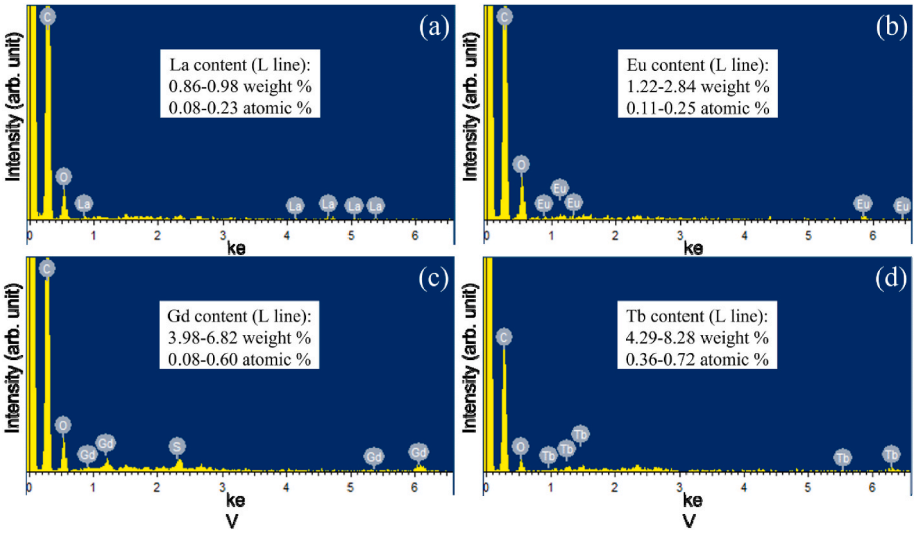

Fig. 10. EDS spectra of (a) GO-La-1, (b) GO-Eu-1, (c) GO-Gd-1, and (d) GO-Tb-1.

with a total disappearance of the C-O signal at 1041 cm^{-1}, an intensity increase of the band due to sp^2 C═C bond vibrations at 1552-1593 cm^{-1}, and the appearance of a band near 1340 cm^{-1} corresponding to stretching C-O bond vibrations in alcohols. As a whole, all the FTIR spectra presented are indicative of structural changes in the oxygen-containing groups of GO, which can be interpreted as pointing to the chemical bonding of Ln ions to GO sheets by replacing H atoms of OH, COOH functionalities or breaking C-O-C bonds where the pH media plays an important role such as for Series 2, where the use of KOH and water media in the solvothermal process fosters the interaction of Ln ions with COOH groups, rather than the interaction with epoxy groups.

Further details of the chemical bonding in GO-Ln samples in

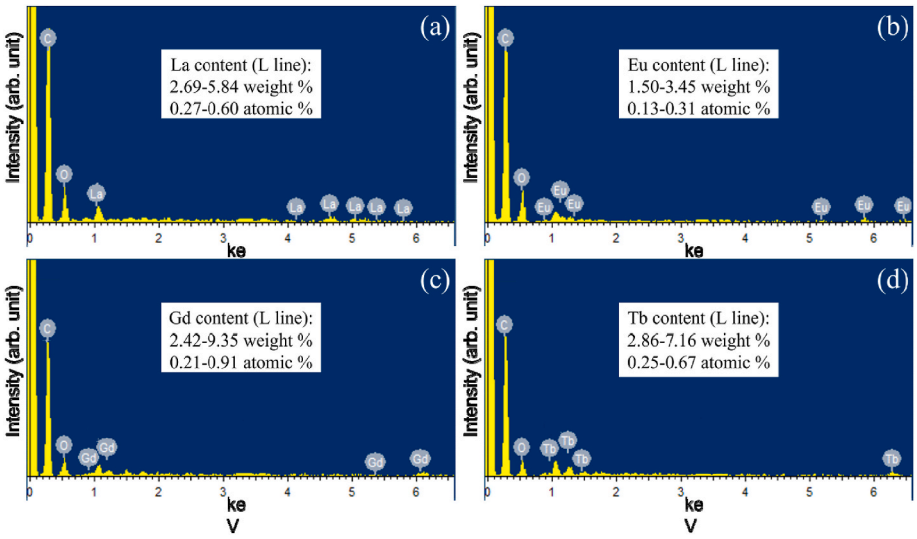

Fig. 11. EDS spectra of (a) GO-La-2, (b) GO-Eu-2, (c) GO-Gd-2, and (d) GO-Tb-2.

comparison to pristine GO were obtained from XPS measurements. XPS spectra of the C1*s*, O1*s* and Ln 3*d* core level regions are shown in Figs. 4–6, respectively; the corresponding binding energies and the percentages indicating the relative at% are listed in Tables S1–S4. The fit of the C1*s* core level spectrum of pristine GO (Fig. 4) requires six components at binding energies (BEs) of 284.2, 285.0, 285.9, 287.2, 288.2 and 289.3 eV, attributed respectively to the presence of CH-CH, C-C, C-CH_2, C-O, C═O and COOH bonds. Their contributions to the total C1*s* spectral intensity amounted to 8.6, 25.8, 16.9, 32.9, 8.5 and 7.5%, respectively. After the solvothermal treatment, with the incorporation of Ln(III) ions on GO, the most remarkable change for both sample series was the appearance of a new component at a BE of 287.5–287.8 eV, attributed to the bond between Ln atoms and GO oxygenated functionalities. The relative contribution of this component to the total C1*s* spectral intensity varies from 6.4% for La to 19.6% for Gd. Although the bonding nature in lanthanide compounds is still under discussion [52], this effect might be linked to the difference in electron configuration of the two lanthanide ions, which is [Xe]$4f^0$ for La^{3+} and [Xe]$4f^7$ for Gd^{3+}. Therefore, with a higher number of 4*f* electrons, the Gd^{3+} ion can exhibit a higher coordination number, i.e. form a larger number of chemical bonds with functional groups in the reaction medium: in the present case, with oxygenated functionalities of GO. To put it in a different way, as the Ln atomic number increases, the ionic radius decreases and hence the charge density of the cation increases, leading to the differences observed. The peak related to C-O for all GO-Ln samples downshifts by approximately 0.6 eV (to 286.5 eV), and the contributions related to C═O and COOH exhibited similar shift higher binding energies, namely to 288.9 and 290.5 eV, respectively, indicating that the integration of Ln ions can also change the electronic charge of oxygen-containing groups of GO. Also, the relative intensity related to the oxygen-containing groups decreases for C-O to 13.5–27.9%, for C═O to 5.4–8.9% and for COOH to 1.7–4.8% of the total C1*s* intensities. It can be said, hence, that the solvothermal conditions promote the chemical reaction of C-O, C═O, and COOH groups to C-O-Ln bonds and change the nature of oxygen functional groups of GO.

The O1*s* (Fig. 5) line of the pristine GO sample can be deconvoluted into four contributions at 531.0, 531.9, 532.6 and 533.5 eV, which are assigned respectively to COOH, C═O, C-OH, and C-O. The contributions amounted of the total O1*s* spectral intensity are 5.0%, 15.5%, 38.4% and 36.6%, respectively. After the solvothermal reactions with the Ln salts, new components appear at 530.5–531.4 eV due to Ln-O bonding and the relative intensity goes from 0.6% to 13.3% of the total O1*s* line intensity depending on the Ln composite, in accordance with the changes observed in C1*s* line. Also, a slight shift of 0.1–0.4 eV can be observed for the peak assigned to the C═O component, while the binding energy of the contribution due to C-OH bonds does not change. Therefore, it can be observed that while the C═O and COOH component shifts to higher BEs in the C1*s* peak, they shift to lower BEs in the O1*s* peak, conversely to the C-O component, confirming the change in electronic distribution in oxygen groups of GO. The relative intensity of C═O varies in the range of 18.4–37.0% between the different Ln composites, decreases for C-OH to 11.9–27.0% and increases for C-O to 20.1–39.8% of the total O1*s* peak. This supports the claim that C-OH groups replace H atoms to form a chemical bonding with Ln ions.

A number of previous studies [53–55] demonstrated that variations in ligand nature and/or coordination number of lanthanides cause changes in relative intensities of satellites and main Ln 3*d* signals. The assignment of final states related to the 3*d* core level peaks is a difficult task due to the existence of satellite features next to the main spectral components. The Ln 3*d* photoemission lines observed for several compounds can be accompanied by shake-up, shake-down and multiplet splittings, which leads to a very complex fine structure [56,57]. In our case, the XPS spectra of the La $3d_{5/2}$ core level for GO-La-1 and GO-La-2 show the main component at 834.8 eV and satellites appearing at about 838.5 and 836.7 eV that are indicative of the presence of La^{3+} [58,59]. The difference between the two samples concerns one more satellite located at a BE of 832.7 eV for GO-La-1, and at 840.5 eV for GO-La-2. The Eu 3*d* XPS spectra for europium-containing samples are qualitatively similar to each other. For GO-Eu-1, the main peaks are observed at 1164.8 eV and 1135.0 eV, respectively, and these binding energies are typical for Eu^{3+} [60]. One can also see minor components at 1156.3 eV and 1126.6 eV, which can be attributed to Eu^{2+} [60], with additional multiplet features at BEs of 1144.0 and 1172.5 eV. For GO-Eu-2, the component located at 1152.3 eV is shifted by 4.0 eV with respect to the Eu^{2+} peak at 1156.3 eV for GO-Eu-1. In the Gd $3d_{5/2}$ core level spectrum for GO-Gd-1, the main peak due [61] to Gd^{3+} appears at 1187.4 eV and its satellite at 1196.0 eV. For GO-Gd-2, the main component is found at 1188.4 eV (1.00 eV higher than for GO-Gd-1) and its satellite at 1197.5 eV. The main peak in the Tb $3d_{5/2}$ spectrum appears at a BE of 1241.7 eV for GO-Tb-1, and at 1241.5 eV for GO-Tb-2, with a multiplet additionally present in the case of GO-Tb-1 sample. All the samples show differences between the BEs components of $3d_{5/2}$ core levels due to the interactions related to oxides and hydroxides.

The atomic percentages of the elements present in all the samples were calculated and are presented in Table S4. The estimated content for La (GO-La-1) is 0.6 at%, for Eu (GO-Eu-1) is 0.8 at%, for Gd (GO-Gd-1) is 0.7 at%, for Tb (GO-Tb-1) is 0.3 at%, for La (GO-La-2) is 0.4 at%, for Eu (GO-Eu-2) is 0.6 at%, for Gd (GO-Gd-2) is 0.9 at%, and for Tb (GO-Tb-2)

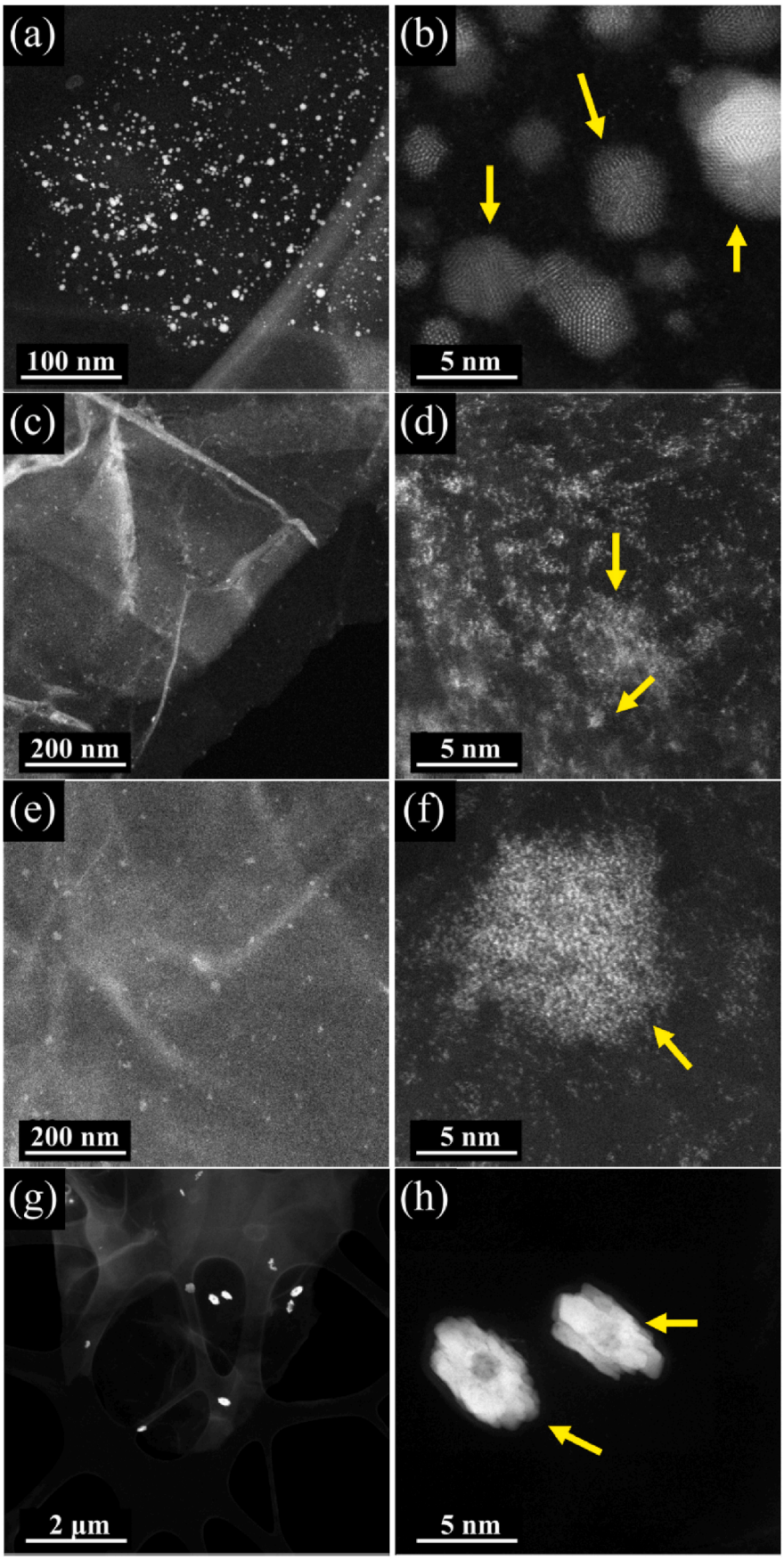

Fig. 12. Dark-field TEM images at different magnifications of (a, b) GO-La-1, (c, d) GO-Eu-1, (e, f) GO-Gd-1, and (g, h) GO-Tb-1. (Yellow arrows point to lanthanide oxide nanoparticles). (For interpretation of the references to colour in this figure legend, the reader is referred to the Web version of this article.)

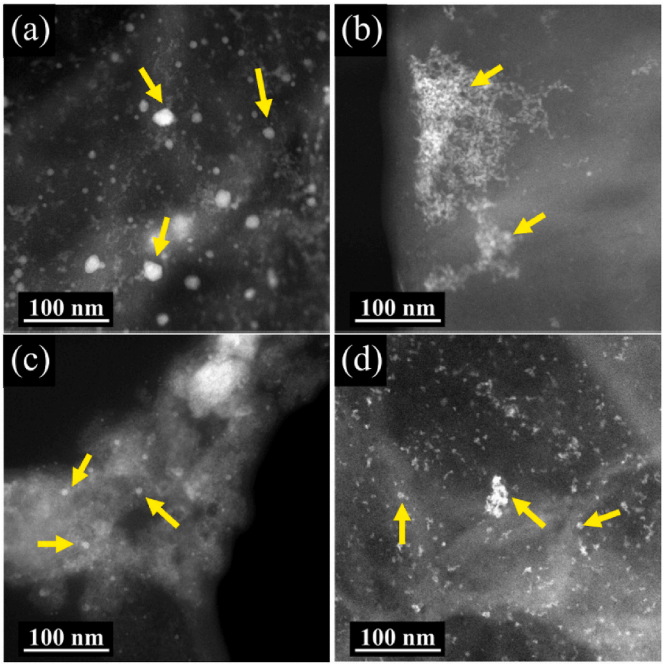

Fig. 13. Dark-field TEM images of (a) GO-La-2, (b) GO-Eu-2, (c) GO-Gd-2, and (d) GO-Tb-2. (Yellow arrows point to lanthanide hydroxide nanoparticles). (For interpretation of the references to colour in this figure legend, the reader is referred to the Web version of this article.)

is 0.5 at%. The amount of lanthanide in the nanocomposites is slightly lower for La^{3+} and Tb^{3+} than for Eu^{3+} and Gd^{3+} in both series, indicating a different nanoparticle formation efficiency. As could be seen with the relative contributions of C-O-Ln components to the total C1*s* intensity, this can be attributed to the differences in the electronic configuration of the four lanthanides used, where also half-filled electron shell effect can influence the ability and stability of bonding with oxygen functionalities of GO.

The XRD pattern of pristine GO (Fig. 7) presents a characteristic sharp peak at 11.4° consistent with a basal spacing of $d_{001} = 7.8$ Å that is associated with the presence of hydroxyl, epoxy, and carbonyl groups and possibly intercalated water between the GO sheet surfaces [50,62]. After the solvothermal reaction, the XRD patterns of GO-Ln samples of both series 1 and 2, show a broad peak that points to exfoliation of the GO sheets; the maximum at around 25.1° corresponds to a basal spacing of $d_{002} = 3.5$ Å that can be explained by a partial reconstruction of the sp^2 carbon network involving the epoxy ring-opening reactions as reported by Fan et al. using aluminum powder [63,64] and agrees with the sp^2 C═C band increase observed in the FTIR results. In the case of GO-Ln-1 samples, no peaks attributable to Ln oxides were observed, which can be explained by the very small dimensions and low crystallinity of Ln nanoparticles formed [65]. At the same time, the diffractograms obtained for GO-Ln-2 samples exhibit a series of characteristic peaks corresponding to the hexagonal crystal structure of lanthanide hydroxides and indicate larger Ln nanoparticles than for GO-Ln-1 [66–69], and it confirms that even using shorter reaction times than Zheng reported [43] it is possible to obtain nanoparticles onto GO surface employing the solvothermal technique.

The morphology of the GO-Ln hybrids was investigated at different length scales with the help of SEM and TEM. SEM images acquired in the backscattered electron composition (BEC) mode, where light and heavy elements appear with different contrast, are presented in Figs. 8 and 9. The micrographs show GO sheets covered by lanthanide-containing particles of variable size as can be seen in the particle distribution histograms (Figs. S1 and S2): for the GO-Ln-1 series, the particle sizes range from approximately 100 to 800 nm with a mean size of (387 ± 127) nm for GO-La-1, (300 ± 48) nm for GO-Eu-1, (472 ± 99) nm for GO-Gd-1, and (357 ± 80) nm, whereas for the GO-Ln-2 series, the particle size varies roughly between 800 and 7000 nm, with a mean size of (2169 ± 203) nm for GO-La-2, (2774 ± 1446) nm for GO-Eu-2, (1170 ± 131) nm for GO-Gd-2, and (935 ± 401) nm for GO-Tb-2. The samples of the GO-Ln-1 series exhibit a much more homogeneous particle distribution compared to the GO-Ln-2 series. There is also a difference between particle shapes: when comparing GO-La-1 and GO-La-2 most striking is the presence of large rod-shaped particles in the latter. The corresponding EDS spectra were probed at 10 different sites, representative results shown in Figs. 10 and 11, S3, and S4 allow to estimate the Ln content, which is as follows: (0.86–0.98) wt% for GO-La-1; (1.22–2.84) wt% for GO-Eu-1; (3.98–6.82) wt% for GO-Gd-1 and (4.29–8.28) wt% for GO-Tb-1; while it was higher for the second series, namely (2.69–5.84) wt% for GO-La-2; (1.50–3.45) wt% for GO-Eu-2; (2.42–9.35) wt% for GO-Gd-2 and (2.86–7.16) wt%, for GO-Tb-2 (see also Table S5). The EDS also confirms that there are no other contaminant species present. The Ln content expressed in at% (see Figs. 10 and 11) agrees with that derived from the XPS results (Table S4) within the experimental error.

For exploring the finer details of the size and distribution of the lanthanide-containing particles, we employed dark-field TEM. The images of GO-Ln-1 and GO-Ln-2 samples are presented in Figs. 12 and 13, respectively. One can see that in addition to the larger particles seen in SEM, nanoparticles are also present in both samples, as illustrated in particle distribution histograms (Figs. S5 and S6). In the case of La, a more uniform distribution on the GO sheets is observed for GO-La-1 (Fig. 12a and b), where the particle size varies in the range of approximately 2–5 nm with a mean size of (3.4 ± 1.3) nm. Similar features are found in the GO-La-2 image (Fig. 13a), with almost equally well-distributed nanoparticles, but their size is notably larger, namely up to *ca.* 20 nm but with a mean size of (8.9 ± 4.2) nm. In both cases, the nanoparticle morphology is close to spherical. The particles appearing in both Eu-containing samples are apparently amorphous and smaller, with a mean size of (0.9 ± 0.5) nm for GO-Eu-1 and (8.2 ± 2.0) nm for GO-Eu-2. Also, a more homogeneous coverage can be observed in the case of GO-Eu-1 (Fig. 12c and d). General similarities were also found between GO-Gd-1 (Fig. 12e and f) and GO-Gd-2 (Fig. 13c), where the nanoparticle structure seems to be amorphous as well, with mean sizes of (1.3 ± 0.6) nm for GO-Gd-1 and (6.6 ± 1.5) nm for GO-Gd-2. On the contrary, the nanoparticles observed in GO-Tb-1 (Fig. 12g and h) exhibit clear facets, forming compact agglomerates of roughly 160 nm but the coverage appears to be scarce compared to the nanoparticle distribution in GO-Tb-2 (Fig. 13d); here, the formations seem to be amorphous as for the Eu- and Gd-containing samples with a mean size of (8.3 ± 3.5) nm. Jenkins et al. [26] used atomic force microscopy to confirm Ln_2O_3 particle size distribution in the nano range: in particular, 10–60 nm for Sm_2O_3 and Dy_2O_3, with some up to 120 nm for Sm_2O_3. Gd_2O_3 particle size ranges from 10 to 42.5 nm, while Er_2O_3 has 50 nm with agglomerated bigger particles around 150 nm. Also, Zhang et al. [28] and Aryanrad et al. [29] confirm La_2O_3 nanorods and Eu_2O_3 nanorods that have a diameter of about 20 nm (by TEM) and 30 nm (by SEM), respectively. That is, our approach allows for the preparation of smaller nanoparticles with a considerably larger surface area. Thus, according to SEM and TEM results together with Raman, FTIR and XPS studies, it can be stated that not only the solvothermal conditions have an important effect on the behaviour of the interaction of Ln ions with oxygen functional groups of GO, the morphology and distribution of lanthanide oxide and hydroxide nanoparticles, but also the nature of the lanthanides itself.

The thermal behaviour of GO-Ln nanocomposites was studied by TGA-DTA analysis; the corresponding thermograms are shown in Fig. 13. The TGA curve for pristine GO (Fig. 14a) exhibits three main weight loss steps. The first loss of 16.7% occurs up to 100 °C and is due to the evaporation of physisorbed water. The second loss of 28.7% is observed until 241 °C and is caused by the decomposition of the intrinsic

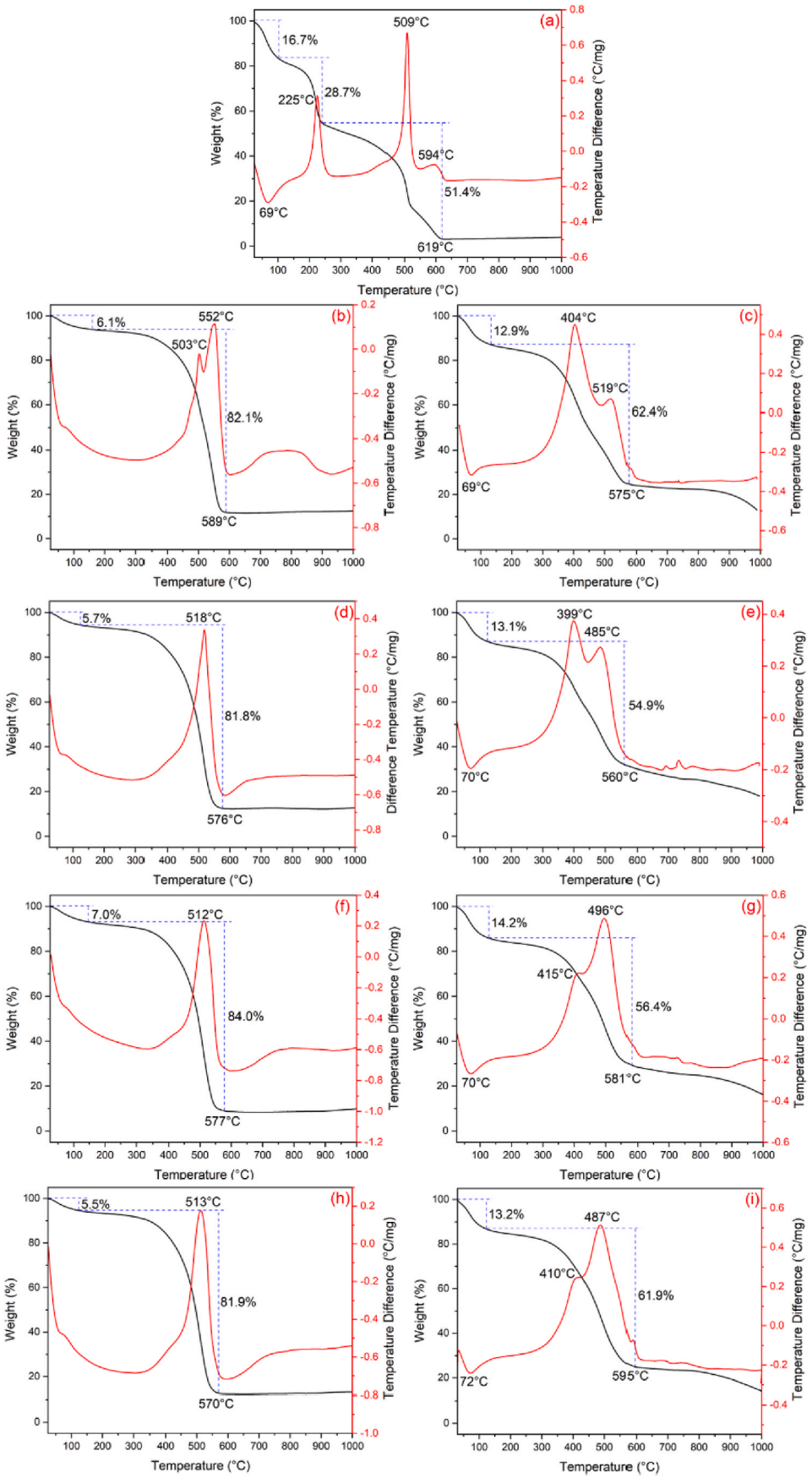

Fig. 14. Comparison of TGA (black) – DTA (red) curves of (a) pristine GO, (b) GO-La-1, (c) GO-La-2, (d) GO-Eu-1, (e) GO-Eu-2, (f) GO-Gd-1, (g) GO-Gd-2, (h) GO-Tb-1 and (i) GO-Tb-2. (For interpretation of the references to colour in this figure legend, the reader is referred to the Web version of this article.)

oxygen-containing groups of GO. The third weight loss of 51.4%, ending at 619 °C, corresponds to the decomposition of the graphene backbone. The DTA thermogram contains features at 69, 225 and 509 °C, consistent with the three weight-loss steps in the TGA curve. The thermograms for GO-Ln-1 composites exhibited only two weight loss steps; the first one (due to the elimination of adsorbed water) amounts to 5.5–7.0% ends at about 120 °C and a similar step can be observed for GO-Ln-2 series as well, but its magnitude is considerably higher, namely 12.9–14.2%. The second weight loss in the TGA curves of the GO-Ln-1 series finishes below 600 °C, *viz*. at 589 °C for GO-La-1, 576 °C for GO-Eu-1, 577 °C for GO-Gd-1 and 570 °C for GO-Tb-1, with the corresponding DTA peaks at 503, 518, 512 and 513 °C. In other words, the thermal stability of Ln-containing samples decreases by 30–60 °C compared to the final decomposition temperature of pristine GO, and this decrease can be attributed to a catalytic effect of lanthanide oxides on the combustion of the graphene backbone. This final weight loss for GO-Ln-1 samples is matched by the second (of a total of three) weight loss step for the GO-Ln-2 series, ending at 575 °C for GO-La-2, at 560 °C for GO-Eu-2, at 581 °C for GO-Gd-2 and at 595 °C for GO-Tb-2; again, the thermal stability of the Ln-containing samples is lower than that of pristine GO. The corresponding DTA thermograms exhibit a more complex structure, with the main maxima observed at lower temperatures than for the GO-Ln-1 series, *i.e.* at 404 °C for GO-La-2, 399 °C for GO-Eu-2, 496 °C for GO-Gd-2 and 487 °C for GO-Tb-2. The final (third) weight loss step for the GO-Ln-2 samples ends at temperatures as high as 1000 °C and represents the main difference between the two series: it confirms the fact that Ln species exist as hydroxides in GO-Ln-2 samples, which are dehydrated at temperatures higher than 600 °C. From the analysis of TGA curves, it is possible to estimate that the lanthanide oxide content; in GO-La-1 it amounts to 11.8%, in GO-Eu-1 to 12.5%, in GO-Gd-1 to 9.0% and in GO-Tb-1 it is 12.6% (Fig. 9). For the GO-Ln-2 series, the values of 22% (La), 25% (Eu), 25% (Gd) and 23% (Tb), roughly approximated from the horizontal ramp at around 700 °C, correspond to Ln hydroxide content. Both for GO-Ln-1 and GO-Ln-2, the estimated Ln content is considerably higher than the values obtained from EDS, and this could be explained due to TGA allowing quantifying not only the content of Ln but the whole Ln oxide content that forms during the thermogravimetric process.

4. Conclusions

We propose a facile time-saving approach to the preparation of GO-Ln_2O_3 and GO-$Ln(OH)_3$ nanocomposites under relatively mild conditions, applying two pathways of solvothermal synthesis. One can suggest that the mechanism of GO-Ln nanocomposite formation involves the initial coordination of Ln^{3+} ions to the oxygen-containing groups of GO as nucleation sites, which is followed by the formation of Ln_2O_3 and $Ln(OH)_3$ nanoparticles. Although FTIR and XRD present an increase in sp^2 hybridized carbon, all the nanocomposites obtained preserve I_D/I_G ratio of sp^3 defects and the intrinsic planar honeycomb-like structures of graphene with the typical G and D bands in the Raman spectra. FTIR and XPS spectra support the interaction between oxygen-containing groups of GO and Ln ions. The size and distribution of Ln oxide/hydroxide nanoparticles on GO sheets, estimated from SEM and TEM images, varies broadly, *e.g.* for the composites with Eu, the size spans from sub-nm dimensions (by TEM) in the case of GO-Eu-1 to more than 10 μm (by SEM) for GO-Eu-2. The most homogeneous distribution of Ln oxide/hydroxide nanoparticles was found in GO-La-1 and GO-La-2. TGA-DTA measurements demonstrated that all the GO-Ln nanocomposites are less thermally stable than pristine GO by up to 30 °C. The results demonstrate that the solvothermal approach is a simple, efficient, and eco-friendly preparation pathway for GO-Ln nanocomposites.

CRediT authorship contribution statement

Diego A. Acevedo-Guzmán: Investigation, Data curation, Formal analysis, Validation, Visualization, Writing – original draft. **Lázaro Huerta:** Investigation, Validation, Visualization. **Monserrat Bizarro:** Investigation, Validation, Visualization. **Víctor Meza-Laguna:** Investigation, Validation, Visualization. **Petra Rudolf:** Supervision, Validation, Visualization, Writing – review & editing. **Vladimir A. Basiuk:** Investigation, Methodology, Validation, Writing – review & editing. **Elena V. Basiuk:** Conceptualization, Methodology, Validation, Supervision, Project administration, Funding acquisition, Writing – review & editing.

Declaration of competing interest

The authors declare that they have no known competing financial interests or personal relationships that could have appeared to influence the work reported in this paper.

Data availability

No data was used for the research described in the article.

Acknowledgements

Financial support from the National Autonomous University of Mexico (UNAM, grant DGAPA-IN100821) is greatly acknowledged. D. A. A.-G. is indebted to the Postgraduate Program in Chemical Sciences of UNAM, the National Council of Science and Technology of Mexico (CONACYT), and the Double-Degree Program of UNAM with the University of Groningen for a PhD scholarship. The authors are also grateful to the University Laboratory of Spectroscopic Characterisation of UNAM (LUCE-ICAT-UNAM) for the use of Raman and FTIR equipment. We thank Josué Esau Romero-Ibarra for the TEM measurements.

Appendix A. Supplementary data

Supplementary data to this article can be found online at https://doi.org/10.1016/j.matchemphys.2023.127840.

References

[1] X. Zhou, X. Huang, X. Qi, S. Wu, C. Xue, F.Y. Boey, Q. Yan, P. Chen, H. Zhang, In situ synthesis of metal nanoparticles on single-layer graphene oxide and reduced graphene oxide surfaces, J. Phys. Chem. C 113 (25) (2009) 10842–10846, https://doi.org/10.1021/jp903821n.
[2] C. Xu, X. Wang, J. Zhu, Graphene– metal particle nanocomposites, J. Phys. Chem. C 112 (50) (2008) 19841–19845, https://doi.org/10.1021/jp807989b.
[3] P.V. Kamat, Graphene-based nanoarchitectures. Anchoring semiconductor and metal nanoparticles on a two-dimensional carbon support, J. Phys. Chem. Lett. 1 (2) (2010) 520–527, https://doi.org/10.1021/jz900265j.
[4] A.L. Jenkins, Polymer-Based Lanthanide Fluorometric Sensors for the Detection of Chemical Agents, Doctoral dissertation). University of Maryland, Baltimore County, 1998.
[5] K. Chen, H. Gao, B. Bai, W. Liu, X. Li, Microwave hydrothermal synthesis of terbium ions complexed with porous graphene for effective absorbent for organic dye, Nanoscale Res. Lett. 12 (1) (2017) 1–8, https://doi.org/10.1186/s11671-017-1962-7.
[6] M. Latva, H. Takalo, V.M. Mukkala, C. Matachescu, J.C. Rodríguez-Ubis, J. Kankare, Correlation between the lowest triplet state energy level of the ligand and lanthanide (III) luminescence quantum yield, J. Lumin. 75 (2) (1997) 149–169, https://doi.org/10.1016/S0022-2313(97)00113-0.
[7] X. Fan, K. Shang, B. Sun, L. Chen, S. Ai, Decoration of surface-carboxylated graphene oxide with luminescent Sm^{3+}-complexes, J. Mater. Sci. 49 (6) (2014) 2672–2679, https://doi.org/10.1007/s10853-013-7975-4.
[8] P. Li, Y. Wang, H. Li, G. Calzaferri, Luminescence enhancement after adding stoppers to europium (III) nanozeolite L, Angew. Chem. Int. Ed. 53 (11) (2014) 2904–2909, https://doi.org/10.1002/anie.201310485.
[9] Y. Chen, Y. Chi, H. Wen, Z. Lu, Sensitized luminescent terbium nanoparticles: preparation and time-resolved fluorescence assay for DNA, Anal. Chem. 79 (3) (2007) 960–965, https://doi.org/10.1021/ac061477h.
[10] V.A. Basiuk, O.V. Prezhdo, E.V. Basiuk, Adsorption of lanthanide atoms on graphene: similar, yet different, J. Phys. Chem. Lett. 13 (2022) 6042–6047, https://doi.org/10.1021/acs.jpclett.2c01580.
[11] X. Liu, C.Z. Wang, M. Hupalo, W.C. Lu, M.C. Tringides, Y.X. Yao, K.M. Ho, Metals on graphene: correlation between adatom adsorption behavior and growth

morphology, Phys. Chem. Chem. Phys. 14 (25) (2012) 9157–9166, https://doi.org/10.1039/C2CP40527J.
[12] Y.J. Li, M. Wang, M.Y. Tang, X. Tian, S. Gao, Z. He, Y. Li, T.G. Zhou, Spin and orbital magnetic moments and spin anisotropy energies of light rare earth atoms embedded in graphene: a first-principles study, Physica E: Low-Dimens. Syst. Nanostruct. 75 (2016) 169–173, https://doi.org/10.1016/j.physe.2015.09.017.
[13] S. Li, M. Zhou, G. Li, F. Zheng, P. Zhang, Strong bonding and high spin-polarization of lanthanide atoms on vacancies in graphene, AIP Adv. 7 (10) (2017), 105207, https://doi.org/10.1063/1.4994714.
[14] V.A. Basiuk, D.A. Acevedo-Guzman, V. Meza-Laguna, E. Alvarez-Zauco, L. Huerta, M. Serrano, M. Kakazey, E.V. Basiuk, High-energy ball-milling preparation and characterization of Ln_2O_3− graphite nanocomposites, Mater. Today Commun. 26 (2021), 102030, https://doi.org/10.1016/j.mtcomm.2021.102030.
[15] A. Rodríguez-Galván, M. Rivera, P. García-López, L.A. Medina, V.A. Basiuk, Gadolinium-containing carbon nanomaterials for magnetic resonance imaging: trends and challenges, J. Cell Mol. Med. 24 (7) (2020) 3779–3794, https://doi.org/10.1111/jcmm.15065.
[16] C. Lee, X. Wei, J.W. Kysar, J. Hone, Measurement of the elastic properties and intrinsic strength of monolayer graphene, Science 321 (5887) (2008) 385–388, https://doi.org/10.1126/science.115799.
[17] K.S. Novoselov, A.K. Geim, S.V. Morozov, D.E. Jiang, Y. Zhang, S.V. Dubonos, I. V. Grigorieva, A.A. Firsov, Electric field effect in atomically thin carbon films, *Science* 306 (5696) (2004) 666–669, https://doi.org/10.1126/science.1102896.
[18] K. Wang, J. Ruan, H. Song, J. Zhang, Y. Wo, S. Guo, D. Cui, Biocompatibility of graphene oxide, Nanoscale Res. Lett. 6 (1) (2011) 1–8, https://doi.org/10.1007/s11671-010-9751-6.
[19] S.F. Kiew, L.V. Kiew, H.B. Lee, T. Imae, L.Y. Chung, Assessing biocompatibility of graphene oxide-based nanocarriers: a review, J. Contr. Release 226 (2016) 217–228, https://doi.org/10.1016/j.jconrel.2016.02.015.
[20] M. Lundie, Ž. Šljivančanin, S. Tomić, Electronic and optical properties of reduced graphene oxide, J. Mater. Chem. C 3 (29) (2015) 7632–7641, https://doi.org/10.1039/C5TC00437C.
[21] M. Rasheed, S. Shihab, O.W. Sabah, An investigation of the structural, electrical and optical properties of graphene-oxide thin films using different solvents, J. Phys.: Conf. Ser. 1795 (1) (2021), 012052, https://doi.org/10.1088/1742-6596/1795/1/012052.
[22] R.M. Ashour, H.N. Abdelhamid, A.F. Abdel-Magied, A.A. Abdel-Khalek, M.M. Ali, A. Uheida, M. Muhammed, X. Zou, J. Dutta, Rare earth ions adsorption onto graphene oxide nanosheets, Solvent Extr. Ion Exch. 35 (2) (2017) 91–103, https://doi.org/10.1080/07366299.2017.1287509.
[23] P.K. Narayanam, K. Sankaran, Luminescence tunability of europium functionalized graphene oxide sheets, Mater. Res. Express 5 (6) (2018), 065039, https://doi.org/10.1088/2053-1591/aaca77.
[24] S. Pang, Z. Zhou, Q. Wang, Terbium-containing graphene oxide and its opto-electrochemical response for hypochlorite in water, Carbon 58 (2013) 232–237, https://doi.org/10.1016/j.carbon.2013.03.004.
[25] Y. Wang, Y. Li, W. Qi, Y. Song, Luminescent lanthanide graphene for detection of bacterial spores and cysteine, Chem. Commun. 51 (55) (2015) 11022–11025, https://doi.org/10.1039/C5CC02889B.
[26] A.L. Jenkins, D.P. Ziegler, E. Emmons, C.J. Karwacki, Preparation and properties of luminescent lanthanide based graphene oxide, J. Phys. Chem. Biophys. 3 (120) (2013), https://doi.org/10.4172/2161-0398.1000120, 2161-0398.
[27] F. Jabeen, M.S. Sajid, B. Fatima, A. Saeed, M.N. Ashiq, M. Najam-ul-Haq, Graphene oxide–metal oxide nanocomposites for on-target enrichment and analysis of phosphorylated biomolecules, J. Separ. Sci. 44 (16) (2021) 3137–3145, https://doi.org/10.1002/jssc.202001276.
[28] J. Zhang, Z. Zhang, Y. Jiao, H. Yang, Y. Li, J. Zhang, P. Gao, The graphene/lanthanum oxide nanocomposites as electrode materials of supercapacitors, J. Power Sources 419 (2019) 99–105, https://doi.org/10.1016/j.jpowsour.2019.02.059.
[29] P. Aryanrad, H.R. Naderi, E. Kohan, M.R. Ganjali, M. Baghernejad, A.S. Dezfuli, Europium oxide nanorod-reduced graphene oxide nanocomposites towards supercapacitors, RSC Adv. 10 (30) (2020) 17543–17551, https://doi.org/10.1039/C9RA11012G.
[30] A. Subasri, K. Balakrishnan, E.R. Nagarajan, V. Devadoss, A. Subramania, Development of 2D $La(OH)_3$/graphene nanohybrid by a facile solvothermal reduction process for high-performance supercapacitors, Electrochim. Acta 281 (2018) 329–337, https://doi.org/10.1016/j.electacta.2018.05.142.
[31] R.K. Sharma, M. Ghora, Y.N. Chouryal, T. Ganguly, D. Acharjee, D.J. Mondal, S. Konar, S. Nigam, P. Ghosh, Multifunctional lanthanide-doped binary fluorides and graphene oxide nanocomposites via a task-specific ionic liquid, ACS Omega 7 (20) (2022) 16906–16916, https://doi.org/10.1021/acsomega.1c06875.
[32] A. Javadi, S. Pan, C. Cao, G. Yao, X. Li, Facile synthesis of 10 nm surface clean TiB2 nanoparticles, Mater. Lett. 229 (2018) 107–110, https://doi.org/10.1016/j.matlet.2018.06.054.
[33] J. Yuan, G. Yao, S. Pan, N. Murali, X. Li, Size control of in situ synthesized TiB 2 particles in molten aluminum, Metall. Mater. Trans. 52 (2021) 2657–2666, https://doi.org/10.1007/s11661-021-06260-2.
[34] P. Lidström, J. Tierney, B. Wathey, J. Westman, Microwave assisted organic synthesis—a review, Tetrahedron 57 (45) (2001) 9225–9283, https://doi.org/10.1016/S0040-4020(01)00906-1.
[35] J.A. Gerbec, D. Magana, A. Washington, G.F. Strouse, Microwave-enhanced reaction rates for nanoparticle synthesis, J. Am. Chem. Soc. 127 (45) (2005) 15791–15800, https://doi.org/10.1021/ja052463g.
[36] F. Bensebaa, N. Patrito, Y. Le Page, P. L'Ecuyer, D. Wang, Tunable platinum–ruthenium nanoparticle properties using microwave synthesis, J. Mater. Chem. 14 (22) (2004) 3378–3384, https://doi.org/10.1039/B404280H.
[37] J. Lai, W. Niu, R. Luque, G. Xu, Solvothermal synthesis of metal nanocrystals and their applications, Nano Today 10 (2) (2015) 240–267, https://doi.org/10.1016/j.nantod.2015.03.001.
[38] S. Chella, P. Kollu, E.V.P. Komarala, S. Doshi, M. Saranya, S. Felix, R. Ramachandran, P. Saravanan, V.L. Koneru, V. Venugopal, S.K. Jeong, A. N. Grace, Solvothermal synthesis of $MnFe_2O_4$-graphene composite—investigation of its adsorption and antimicrobial properties, Appl. Surf. Sci. 327 (2015) 27–36, https://doi.org/10.1016/j.apsusc.2014.11.096.
[39] Y.J. Tong, L.D. Yu, J. Zheng, G. Liu, Y. Ye, S. Huang, G. Ouyang, Graphene oxide-supported lanthanide metal–organic frameworks with boosted stabilities and detection sensitivities, Anal. Chem. 92 (23) (2020) 15550–15557, https://doi.org/10.1021/acs.analchem.0c03562.
[40] B. Gersten, Solvothermal synthesis of nanoparticles, Chemfiles 5 (2005) 11–12.
[41] Z. Li, X. Li, Y. Zong, G. Tan, Y. Sun, Y. Lan, M. He, Z. Ren, X. Zheng, Solvothermal synthesis of nitrogen-doped graphene decorated by superparamagnetic Fe3O4 nanoparticles and their applications as enhanced synergistic microwave absorbers, Carbon 115 (2017) 493–502, https://doi.org/10.1016/j.carbon.2017.01.036.
[42] C. Wang, K. Yang, X. Wei, S. Ding, F. Tian, F. Li, One-pot solvothermal synthesis of carbon dots/Ag nanoparticles/TiO2 nanocomposites with enhanced photocatalytic performance, Ceram. Int. 44 (18) (2018) 22481–22488, https://doi.org/10.1016/j.ceramint.2018.09.017.
[43] H. Zheng, Z. Ji, K.R. Roy, M. Gao, Y. Pan, X. Cai, L. Wang, W. Li, C.H. Chang, C. Chitrada Kaweeteerawat, C. Chen, T. Tian Xia, Y. Zhao, R. Li, Engineered graphene oxide nanocomposite capable of preventing the evolution of antimicrobial resistance, ACS Nano 13 (10) (2019) 11488–11499, https://doi.org/10.1021/acsnano.9b04970.
[44] J.F. Moulder, W.F. Stickle, P.E. Sobol, Handbook of X-Ray Photoelectron Spectroscopy: a Reference Book of Standard Spectra for Identification and Interpretation of XPS Data, Physical Electronics, Eden Praire, MN (USA), 1995.
[45] J.H. Scofield, Hartree-Slater subshell photoionization cross-sections at 1254 and 1487 eV, J. Electron. Spectrosc. Relat. Phenom. 8 (2) (1976) 129–137, https://doi.org/10.1016/0368-2048(76)80015-1.
[46] A. Kaniyoor, S. Ramaprabhu, A Raman spectroscopic investigation of graphite oxide derived graphene, AIP Adv. 2 (3) (2012), 032183, https://doi.org/10.1063/1.4756995.
[47] R. Kumar, B.R. Mehta, M. Bhatnagar, S. Mahapatra, S. Salkalachen, P. Jhawar, Graphene as a transparent conducting and surface field layer in planar Si solar cells, Nanoscale Res. Lett. 9 (1) (2014) 1–9, https://doi.org/10.1186/1556-276X-9-349.
[48] L. Xu, L. Cheng, Graphite oxide under high pressure: a Raman spectroscopic study, J. Nanomater. (2013), https://doi.org/10.1155/2013/731875, 013.
[49] Z. Ni, Y. Wang, T. Yu, Z. Shen, Raman spectroscopy and imaging of graphene, Nano Res. 1 (4) (2008) 273–291, https://doi.org/10.1007/s12274-008-8036-1.
[50] M. Acik, G. Lee, C. Mattevi, A. Pirkle, R.M. Wallace, M. Chhowalla, K. Cho, Y. Chabal, The role of oxygen during thermal reduction of graphene oxide studied by infrared absorption spectroscopy, J. Phys. Chem. C 115 (40) (2011) 19761–19781, https://doi.org/10.1021/jp2052618.
[51] S. Chaiyakun, N. Witit-Anun, N. Nuntawong, P. Chindaudom, S. Oaew, C. Kedkeaw, P. Limsuwan, Preparation and characterization of graphene oxide nanosheets, Procedia Eng. 32 (2012) 759–764, https://doi.org/10.1016/j.proeng.2012.02.009.
[52] T. Vitova, P.W. Roesky, S. Dehnen, Open questions on bonding involving lanthanide atoms, Commun. Chemistry 5 (1) (2022) 12, https://doi.org/10.1038/s42004-022-00630-6.
[53] O.P. Ivanova, L.A. Vasilyev, A.V. Naumkin, V.V. Kantsel, XPS studies of natural monazite and relative compounds under ion bombardment, Appl. Surf. Sci. 72 (4) (1993) 307–312, https://doi.org/10.1016/0169-4332(93)90367-K.
[54] Y.A. Teterin, A.Y. Teterin, A.M. Lebedev, K.E. Ivanov, Secondary electronic processes and the structure of X-ray photoelectron spectra of lanthanides in oxygen-containing compounds, J. Electron. Spectrosc. Relat. Phenom. 137 (2004) 607–612, https://doi.org/10.1016/j.elspec.2004.02.016.
[55] H. Berthou, C.K. Jørgensen, C. Bonnelle, Influence of the ligands on 3d photoelectron spectra of the first four lanthanides, Chem. Phys. Lett. 38 (2) (1976) 199–206, https://doi.org/10.1016/0009-2614(76)85135-4.
[56] A. Novosselov, E. Talik, A. Pajaczkowska, An X-ray photoelectron spectroscopy study on electron structure of some Ln-containing (Ln= La, Pr, Nd and Gd) oxide crystals, J. Alloys Compd. 351 (1–2) (2003) 50–53, https://doi.org/10.1016/S0925-8388(02)01064-2.
[57] B. Glorieux, R. Berjoan, M. Matecki, A. Kammouni, D. Perarnau, XPS analyses of lanthanides phosphates, Appl. Surf. Sci. 253 (6) (2007) 3349–3359, https://doi.org/10.1016/j.apsusc.2006.07.027.
[58] M.F. Sunding, K. Hadidi, S. Diplas, O.M. Løvvik, T.E. Norby, A.E. Gunnæs, XPS characterisation of in situ treated lanthanum oxide and hydroxide using tailored charge referencing and peak fitting procedures, J. Electron. Spectrosc. Relat. Phenom. 184 (7) (2011) 399–409, https://doi.org/10.1016/j.elspec.2011.04.002.
[5][9]] J.P.H. Li, X. Zhou, Y. Pang, L. Zhu, E.I. Vovk, L. Cong, Y. Yang, Understanding of binding energy calibration in XPS of lanthanum oxide by in situ treatment, Phys. Chem. Chem. Phys. 21 (40) (2019) 22351–22358, https://doi.org/10.1039/C9CP04187G.
[60] F. Mercier, C. Alliot, L. Bion, N. Thromat, P. Toulhoat, XPS study of Eu (III) coordination compounds: core levels binding energies in solid mixed-oxo-compounds EumXxOy, J. Electron. Spectrosc. Relat. Phenom. 150 (1) (2006) 21–26, https://doi.org/10.1016/j.elspec.2005.08.003.

[61] D. Raiser, J.P. Deville, Study of XPS photoemission of some gadolinium compounds, J. Electron. Spectrosc. Relat. Phenom. 57 (1) (1991) 91–97, https://doi.org/10.1016/0368-2048(91)85016-M.
[62] A.B. Bourlinos, D. Gournis, D. Petridis, T. Szabó, A. Szeri, I. Dékány, Graphite oxide: chemical reduction to graphite and surface modification with primary aliphatic amines and amino acids, Langmuir 19 (15) (2003) 6050–6055, https://doi.org/10.1021/la026525h.
[63] Z. Fan, K. Wang, T. Wei, J. Yan, L. Song, B. Shao, An environmentally friendly and efficient route for the reduction of graphene oxide by aluminum powder, Carbon 48 (5) (2010) 1686–1689, https://doi.org/10.1016/j.carbon.2009.12.063.
[64] K. Muthoosamy, R.G. Bai, I.B. Abubakar, S.M. Sudheer, H.N. Lim, H.S. Loh, N. M. Huang, C.H. Chia, S. Manickam, Exceedingly biocompatible and thin-layered reduced graphene oxide nanosheets using an eco-friendly mushroom extract strategy, Int. J. Nanomed. 10 (2015) 1505, https://doi.org/10.2147/IJN.S75213.
[65] H.R. Naderi, M.R. Ganjali, A.S. Dezfuli, High-performance supercapacitor based on reduced graphene oxide decorated with europium oxide nanoparticles, J. Mater. Sci. Mater. Electron. 29 (4) (2018) 3035–3044, https://doi.org/10.1007/s10854-017-8234-2.
[66] C.G. Hu, H. Liu, W.T. Dong, Y.Y. Zhang, G. Bao, C.S. Lao, Z.L. Wang, $La(OH)_3$ and La_2O_3 nanobelts—synthesis and physical properties, Adv. Mater. 19 (3) (2007) 470–474, https://doi.org/10.1002/adma.200601300.
[67] J.G. Kang, Y. Jung, B.K. Min, Y. Sohn, Full characterization of $Eu(OH)_3$ and Eu_2O_3 nanorods, Appl. Surf. Sci. 314 (2014) 158–165, https://doi.org/10.1016/j.apsusc.2014.06.165.
[68] J.G. Kang, B.K. Min, Y. Sohn, Synthesis and characterization of $Gd(OH)_3$ and Gd_2O_3 nanorods, Ceram. Int. 41 (1) (2015) 1243–1248, https://doi.org/10.1016/j.ceramint.2014.09.053.
[69] Y. Sohn, Structural and spectroscopic characteristics of terbium hydroxide/oxide nanorods and plates, Ceram. Int. 40 (9) (2014) 13803–13811, https://doi.org/10.1016/j.ceramint.2014.05.096.